

Final Report, Project #21069

Incorporation of Salton Sea Imaging Project data into joint inversions for Vp and Vs models and model assessment via wavefield simulations

PI Clifford Thurber
University of Wisconsin-Madison
March 14, 2022

Research accomplished

The main goals of our work under award #21069 have been to (1) make improvements to the Fang et al. (2016) joint inversion code to remediate problems with the code that were identified during our 2020 SCEC project (award #20040), (2) augment the data set used in the joint inversion, (3) update the joint inversion model utilizing the improved inversion code and expanded data set, and (4) evaluate the new model using wavefield simulations. Here we describe our accomplishments for each of these project goals.

(1) One of the important outcomes from our 2020 SCEC project (award #20040) was the identification of some problems and weaknesses of the Fang et al. (2016) joint inversion code. We have made a major improvement to the code by replacing the pseudo-bending travel time calculator (Um and Thurber, 1987; Koketsu and Sekine, 1998) with a more accurate finite-difference (FD) travel time calculator (Podvin and Lecomte, 1991). We use the "sphere-in-a-box" parameterization (Flanagan et al., 2000) to account for the sphericity of the Earth for regional-scale models. Our tests show that the FD method can properly handle the very large and sharp lateral and vertical velocity changes that are present in southern California seismic velocity models such as CVM-H and CVM-S. A second modification we have made concerns the weighting parameter used to balance the contribution of body-wave versus surface-wave data to the joint inversion. Fang et al. (2016) set a constant balance value for all iterations based on the relative amount and *a priori* uncertainties of the body-wave and surface-wave data. Our new strategy is to use the ratio of the weighted body-wave and surface-wave residuals, updated at each iteration, as the relative weighting. Our synthetic tests show that this dynamic weighting strategy better balances the contributions of the two data types compared to the original weighting strategy of Fang et al. (2016).

(2) Our previous surface-wave data set included a relatively small data set from Fang et al. (2016), with 30,377 Rayleigh wave group travel times with periods ranging from 3 to 12 s. We tried including a much larger data set from previous SCEC-supported work (Thurber and Allam, 2017), with 223,975 Rayleigh wave group travel times with periods ranging from 0.5 to 15 s. Upon examining the residuals from the combined data set, we found a much larger misfit of 1.9 s compared to 1.3 s for the previous result. This motivated us to replace the surface-wave data set with a very large, high-quality data set from Qiu et al. (2019), with 165,261 Rayleigh wave phase travel times in the period range from 2.5 to 16 s (Figure 1). The final misfit from the joint inversion using the Qiu et al. (2019) surface-wave data is 1.3 s, the same as for our original inversion but in the new case with 5 times as much surface-wave data.

(3) Representative depth slices from the new model compared to the Fang et al. (2016) model are shown in Figure 2. Overall, the amplitudes of the velocity variations are visibly greater in the new model. Strong low velocities are evident in both the greater LA Basin area and the Salton Trough region in the northwest and southeast corners of the model, respectively. Although we are reluctant to take the ratio of these Vp and Vs models to determine Vp/Vs given the different resolution quality of the two models, the results are consistent with relatively high Vp/Vs in the greater LA Basin area (which is only partially covered by our current model domain) and the Salton Trough region.

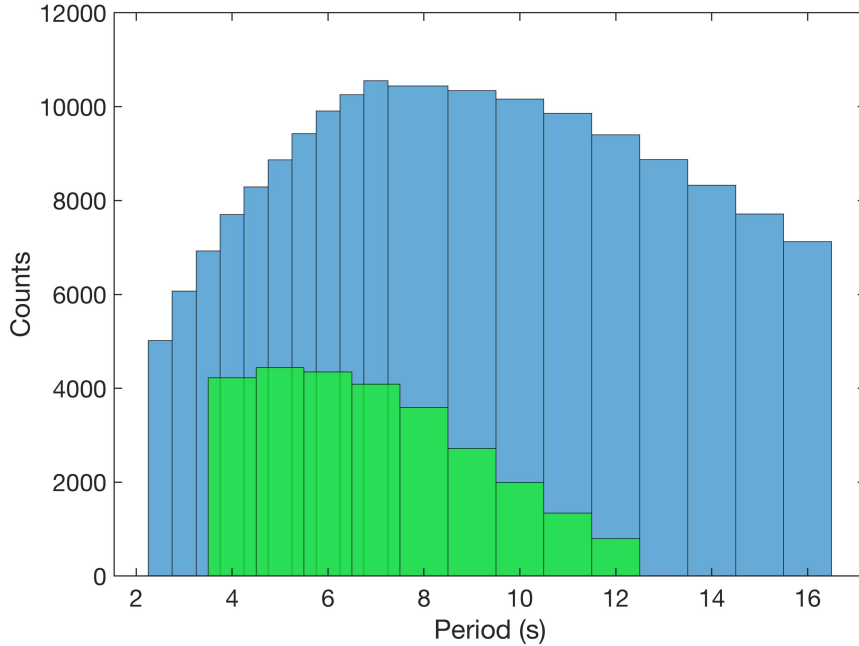


Figure 1. Comparison between the number of Rayleigh wave travel times between station pairs in the previous dataset versus the expanded dataset. The green bars represent the number of travel times in different frequency bins used by Fang et al. (2016), which were taken from Zigone et al. (2014). The blue bars represent the expanded dataset, from Qiu et al. (2019).

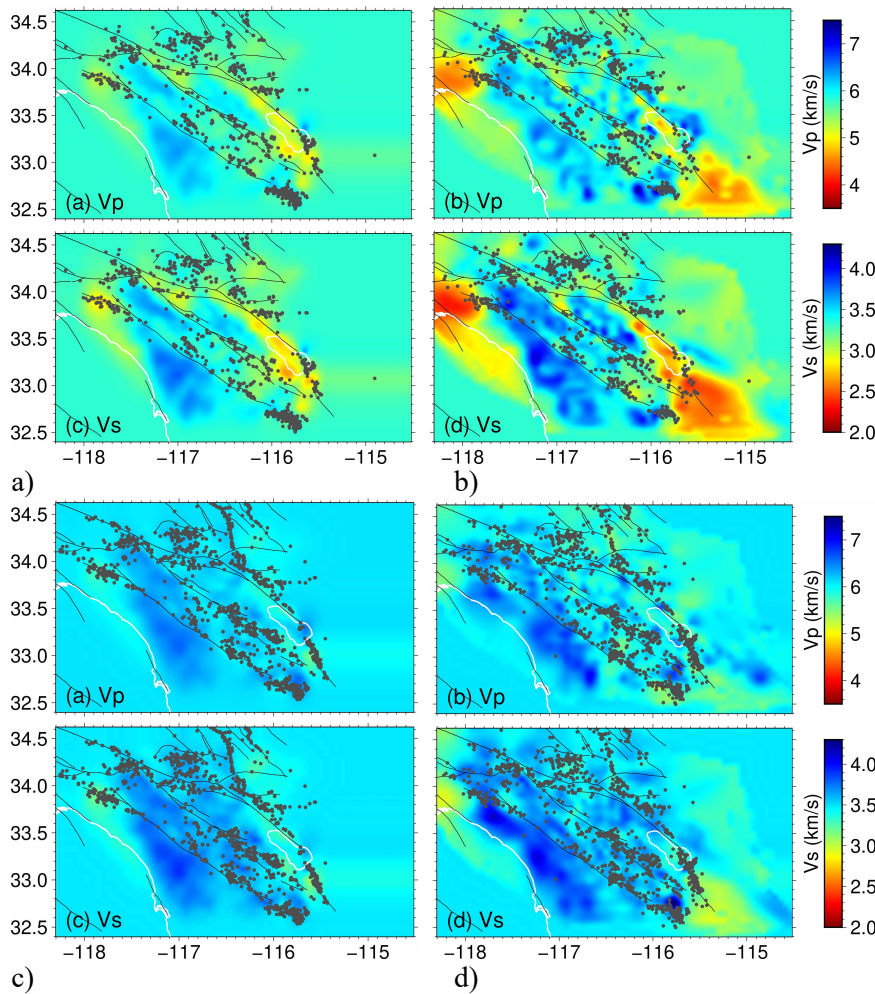


Figure 2. Comparison of depth slices of Vp and Vs at 4 and 8 km depth from (a, c) the original Fang et al. (2016) model and (b, d) the model obtained from the improved joint inversion code and the higher-quality surface-wave dataset of Qiu et al. (2019). Note the low velocities in the greater LA Basin area and Salton Trough region in the northwest and southeast corners of the model, respectively. Black lines are faults, and the coastline and Salton Sea are shown by white lines.

(4) Our next step was the assessment of the new model relative to the previous model. One very simple way to view model adequacy in fitting ambient noise surface-wave data is to plot lines connecting station pairs with the color of the line representing whether the model is too slow or too fast in an area illuminated by crossing paths for a representative range of periods. A similar strategy can be applied to body-wave data. An example for 3 s surface waves in the San Bernardino Basin (SBB) area is shown in Figure 3, with red lines indicating where the model is too fast and blue lines indicating where the model is too slow. We see that the SBB area is mainly crossed red and orange lines, indicating the model is too fast there at 3 s period. Such simple visualizations of model misfit guide our choice of event and station distribution for the formal assessment of the new model via wavefield simulation.

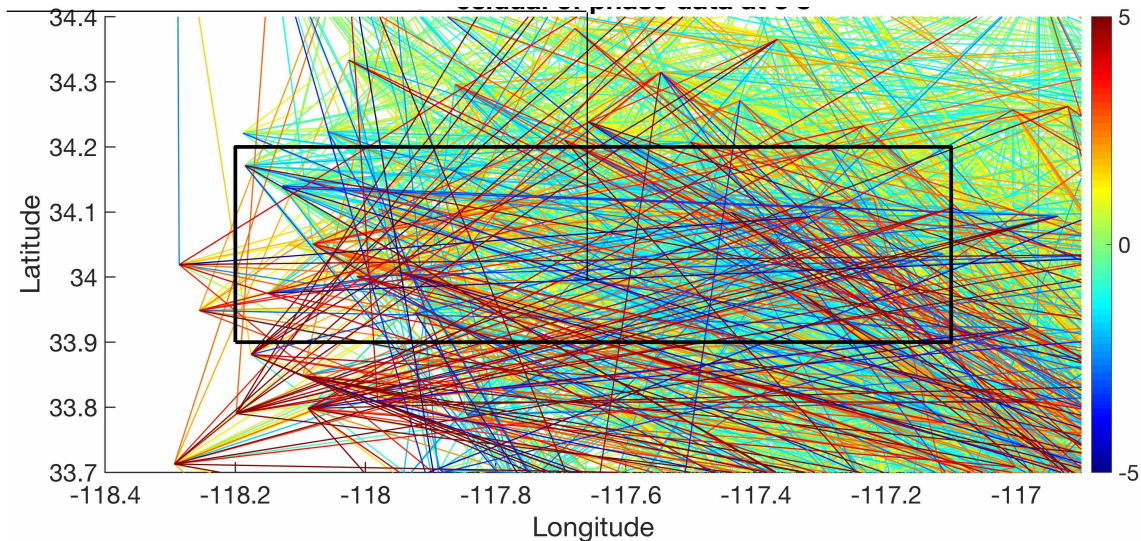


Figure 3. Lines connecting station pairs for ambient noise cross-correlation surface-wave phase data at a period of 3 s for the area of San Gabriel and San Bernardino Valleys, indicated by the black box. Note the preponderance of red and yellow lines in the box, indicating the model velocities need to be decreased to fit the data.

Using a pre-existing framework for CVM-H forward synthetic model runs using SPECFEM3D (Komatitsch et al., 2004; see Toward Full Waveform Tomography Across California (Year 2), Final Report, Project #19017), we were able to create synthetic waveforms for models based on the Fang et al. (2016) results and the updated results presented here (hereafter referred to as the Guo model). To create a velocity model for SPECFEM3D, we embedded the smaller models of Fang et al. (2016) and Guo within the broader CVM-H model. This embedding procedure involved adopting the velocities from Fang et al./Guo in regions characterized by high derivative-weight-sum. In areas of poor coverage in the Fang et al./Guo model, the 3D CVM-H velocity anomalies are preserved. An example of the embedding result for the Guo model is shown in Figure 4. We note that the 3D CVM-H model was not used as the starting model for the Fang et al./Guo model inversions and hence these features were not present in the inverted models due to poor data coverage in these regions.

With the new model now populating the SPECFEM3D mesh, the wavefield simulations are carried out using a selected set of moderate-size earthquakes with well-constrained moment tensors. The time-frequency misfit analysis approach of Kristeková et al. (2006) is then used for model evaluation, comparing the effectiveness of the previous model to the new model. One example is shown in Figure 5. The envelope fit improvement is modest at 12% reduction, from 0.58 to 0.51. However, the reduction in phase misfit is substantial at over 45%, from 0.45 to 0.24, indicating a marked improvement in Rayleigh-wave travel time accuracy. The difference in improvement between the envelope and phase is obvious in the respective "heat maps," with comparable color intensities after 40 s for the envelope plots but a great reduction in size and intensity of the areas of misfit, especially before 70 s.

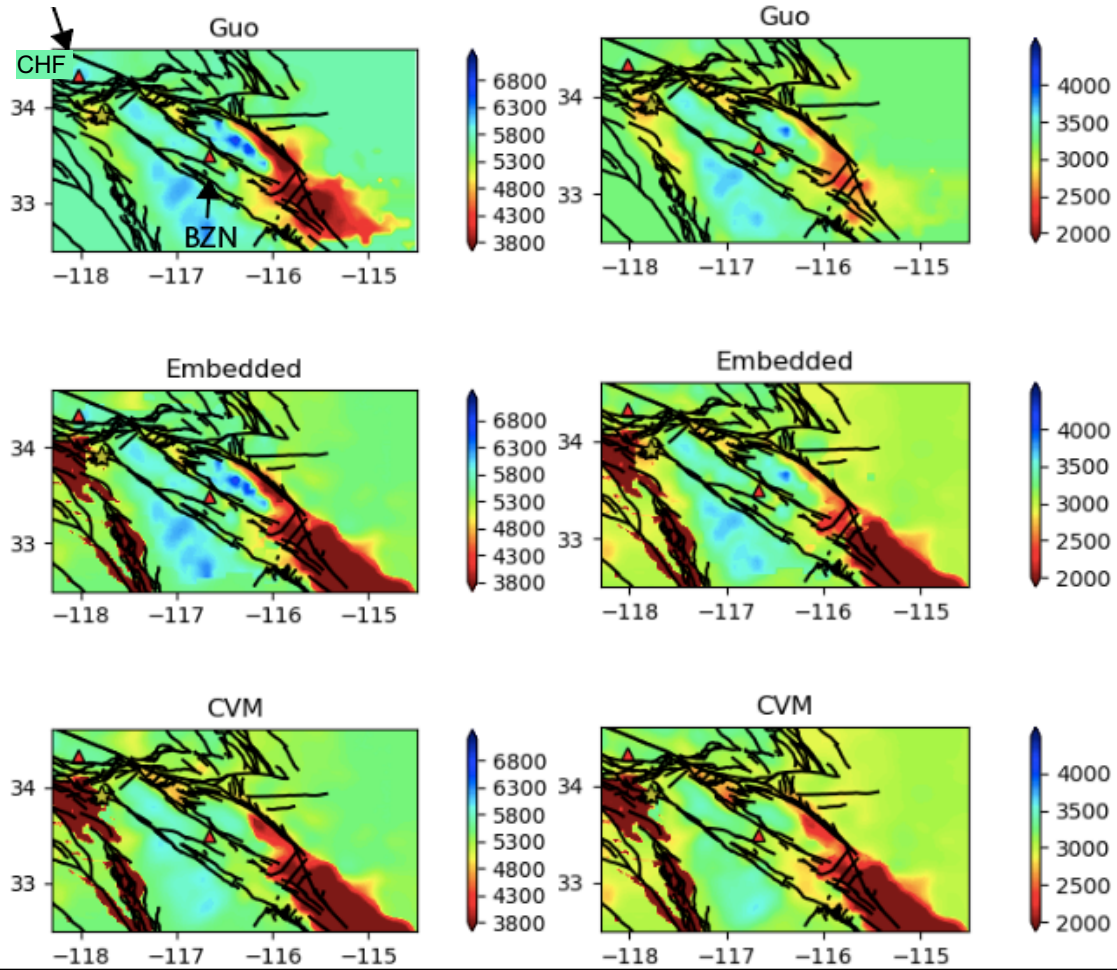


Figure 4. Comparison between the Guo model (top), the Guo embedded model (middle) and the CVM-H model (bottom) for V_p (left column) and V_s (right column) at 2 km depth. The embedded model combines the well resolved portions of the Guo model with the broader 3D velocity coverage of the CVM-H model. Stations CHF and BZN (labeled top left) are plotted as red triangles. The event epicenter, near CHF, is plotted with a gold star. Velocity units are m/s.

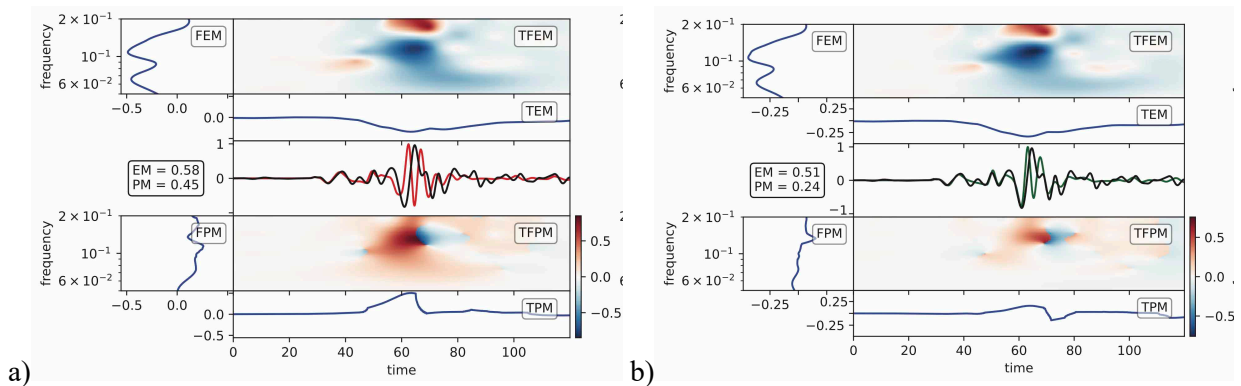


Figure 5. Time-frequency analysis comparing misfit of envelope (EM, top panels) and phase (PM, bottom panels) for Z-component seismograms at station BEL (center panels - black trace is data, colored trace is synthetic) for (a) the Fang et al. (2016) model and (b) our new joint inversion model.

Another example is shown in Figure 6. Here all three components are shown, with the Fang model results on top and the results from the new model below. The reduction in envelope misfit is about 20%, from an average of 0.57 to 0.45. Once again, the reduction in phase misfit is substantial at about 41%, from an average of 0.44 to 0.26, indicating a marked improvement in Rayleigh-wave travel time accuracy. This improvement is quite evident to the eye.

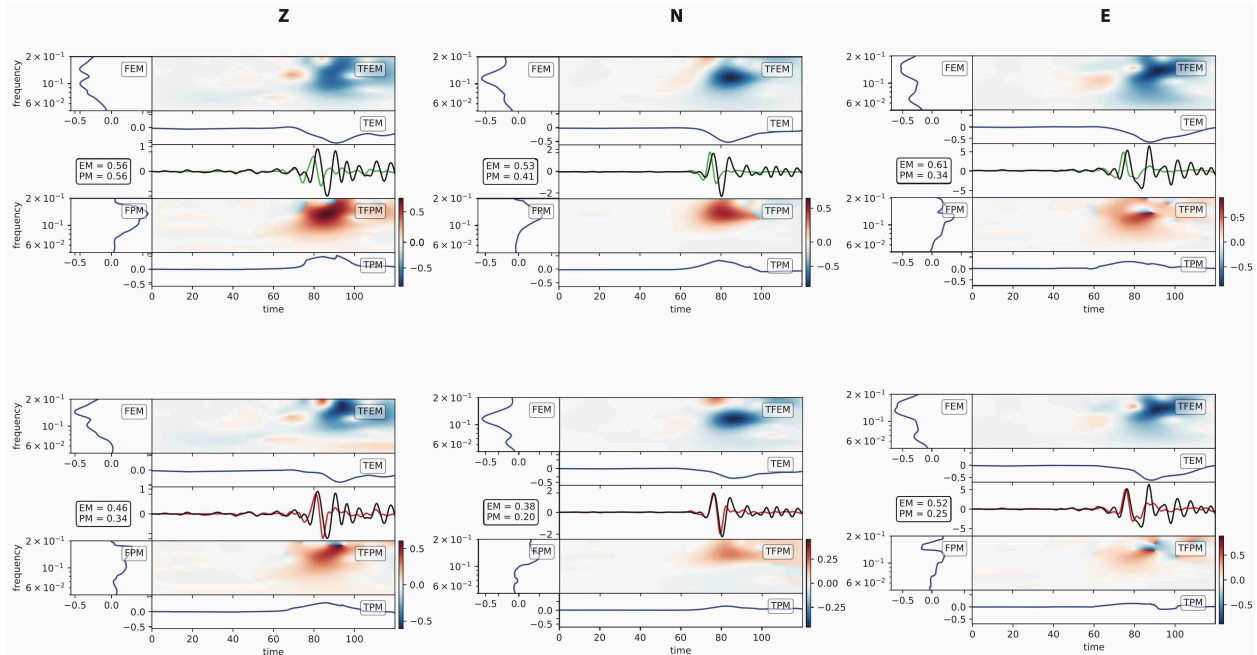


Figure 6. Time-frequency analysis comparing misfit of envelope (EM, top panels) and phase (PM, bottom panels) for three-component seismograms at station SWS (center panels - black trace is data, colored trace is synthetic) for (top) the Fang et al. (2016) model and (bottom) our new joint inversion model.

We conclude that the joint body wave-surface wave inversion approach for updating a 3-D velocity model using an expanded data set is able to yield measurable improvements to the wavefield simulations. We have proposed further work focusing in detail on the San Bernardino Basin area, where we will combine a subset of our current data set with dense observations in and around San Bernardino Basin to produce a higher resolution and higher quality model for that basin.

References

- Fang, H., H. Zhang, H. Yao, A. Allam, D. Zigone, Y. Ben-Zion, C. Thurber, and R. D. van der Hilst (2016), A new algorithm for three-dimensional joint inversion of body-wave and surface-wave data and its application to the Southern California Plate Boundary Region, *J. Geophys. Res. Solid Earth*, 121, doi:10.1002/2015JB012702.
- Flanagan, M. P., S. C. Myers, C. A. Schultz, M. E. Pasyanos, and J. Bhattacharyya (2000), Three-dimensional a priori model constraints and uncertainties for improving seismic location, *Proc. 22nd Seismic Research Review: Technologies for Monitoring the CTBT*, 2-15.
- Koketsu, K., and S. Sekine, (1998), Pseudo-bending method for three-dimensional seismic ray tracing in a spherical earth with discontinuities, *Geophys. J. Int.*, 132, 339-346.
- Komatitsch, D., Q. Liu, J. Tromp, P. Süß, C. Stidham, and J. H. Shaw (2004), Simulations of ground motion in the Los Angeles basin based upon the spectral-element method, *Bull. Seismol. Soc. Am.*, 94, 187-206, doi:10.1785/0120030077.
- Kristeková, M., J. Kristek, P. Moczo, and S. M. Day (2006), Misfit criteria for quantitative comparison of seismograms, *Bull. Seism. Soc. Am.*, 96, 1836-1850.
- Podvin, P. and I. Lecomte (1991), Finite difference computation of travel times in very contrasted velocity models: a massively parallel approach and its associated tools, *Geophys. J. Int.* 105, 271-284.
- Qiu, H., Lin, F.-C., & Ben-Zion, Y. (2019), Eikonal tomography of the Southern California plate boundary region, *J. Geophys. Res.: Solid Earth*, 124, 9755– 9779. <https://doi.org/10.1029/2019JB017806>
- Thurber, C., and A. Allam (2017), Development and validation of an improved seismic velocity model for the San Jacinto fault region, *SCEC Final Project Report #16226*, 6 pp.
- Um, J., and C. H. Thurber (1987), A fast algorithm for two-point seismic ray tracing, *Bull. Seism. Soc. Am.*, 77, 972-986.
- Zigone, D., Y. Ben-Zion, M. Campillo, and P. Roux (2015), Seismic tomography of the southern California plate boundary region from noise-based Rayleigh and Love waves, *Pure Appl. Geophys.*, 172, 1007-1032.